SCIENTIFIC REPORTS
nature research

OPEN

# Symmetry-protected metallic and topological phases in penta-materials

Received: 27 March 2019
Accepted: 20 August 2019
Published online: 04 September 2019

Sergio Bravo[1], Julián Correa[2], Leonor Chico[3] & Mónica Pacheco[1]

**We analyze the symmetry and topological features of a family of materials closely related to penta-graphene, derived from it by adsorption or substitution of different atoms. Our description is based on a novel approach, called topological quantum chemistry, that allows to characterize the topology of the electronic bands, based on the mapping between real and reciprocal space. In particular, by adsorption of alkaline (Li or Na) atoms we obtain a nodal line metal at room temperature, with a continuum of Dirac points around the perimeter of the Brillouin zone. This behavior is also observed in some substitutional derivatives of penta-graphene, such as penta-$PC_2$. Breaking of time-reversal symmetry can be achieved by the use of magnetic atoms; we study penta-$MnC_2$, which also presents spin-orbit coupling and reveals a Chern insulator phase. We find that for this family of materials, symmetry is the source of protection for metallic and nontrivial topological phases that can be associated to the presence of fractional band filling, spin-orbit coupling and time-reversal symmetry breaking.**

Topological phases of materials due to spatial and non spatial symmetries are the subject of enormous attention, both from the fundamental and the applied viewpoint. Firstly, this is because of the promising features related to the presence of robust states at boundaries, such as protected surface states, and also due to the appearance of novel quantum phenomena, showing unique signatures in the electronic transport, optical response and other experimentally relevant magnitudes for applications[1–4].

The search for materials with such desirable properties requires the concurrence of symmetry reasoning along with *ab initio* calculations. On one side, symmetry constrains in a clear and unambiguously way what kind of physical magnitudes are good quantum numbers to classify the states in the system, both in direct and momentum space. On the other side, first-principles approaches allow for the quantitative characterization of the electronic structure of the material. Combining these two basic ingredients, we can tailor properties of materials by design, in order to engineer topological nontrivial phases[5–7].

Different approaches have been proposed to classify topological phases of matter, based on symmetry and combinatorial methods[8–10]. One of the most general and promising theoretical frameworks available for the study of novel materials is the so-called topological quantum chemistry (TQC)[11–13]. This theory combines the non-local description of reciprocal space, in terms of bands, with the local, real space characterization employing atomic orbitals. It allows to classify the universal properties of all possible band structures of weakly correlated materials, making possible the identification of the topological nature of their bands.

In this work, we apply this novel approach to a family of two-dimensional (2D) materials related to penta-graphene (PG). This theoretically predicted carbon allotrope consists of a pentagonal, two-dimensional buckled lattice structure composed only of carbon atoms, first proposed by Tang *et al.*[14] and later by Zhang *et al.*[15]. A variety of penta-materials have been theoretically put forward[16–19], but experimental realizations are certainly scarce for the time being[20,21].

Lately, PG has received considerable attention from different perspectives; it is a quasi-direct gap semiconductor that can be optimally combined with graphene and other 2D materials. Its potential applications have been recently explored[22–28], as well as the possibility of functionalization, adsorption and atomic substitution with the aim of modifying its properties[29–35]. Some of these modifications may change the semiconducting character of

[1]Universidad Técnica Federico Santa María, Departamento de Física, Valparaíso, Chile. [2]Universidad de Medellín, Facultad de Ciencias Básicas, Medellín, Colombia. [3]Materials Science Factory, Instituto de Ciencia de Materiales de Madrid (ICMM), Consejo Superior de Investigaciones Científicas (CSIC), C/Sor Juana Inés de la Cruz 3, 28049, Madrid, Spain. Correspondence and requests for materials should be addressed to M.P. (email: monica.pacheco@usm.cl)

PG, resulting in the appearance of metallic behavior. This feature has been presented in previous works[32,35]; but most importantly, a general symmetry and topological study of these materials is still lacking.

In what follows, we present a complete TQC analysis and *ab initio* calculations that explore the topological nature of these penta-materials, analyzing them from the unifying perspective of group theory.

We study their different phases upon inclusion of spin-orbit interaction and breaking of time-reversal symmetry. We find an evolution of the electronic band structure from a general nodal line located at the boundary of Brillouin zone (BZ), through a point-like Dirac node near the Fermi level at the corner of the BZ, to topologically nontrivial phases in presence of spin-orbit coupling (SOC) plus time-reversal symmetry (TRS) breaking. These different phases are realized separately for specific penta-materials by means of first-principles calculations.

This work is organized as follows. We first perform an analysis for the space group of symmetry transformations present in this family of materials. Next, a topological study is developed using the TQC approach. Certain characteristics of the materials, independent of their specific details, are derived from symmetry and topological analysis. Subsequently, we corroborate our study by means of density-functional theory calculations for several proposed penta-materials, in order to illustrate the realization of the predicted phases. Finally, global conclusions pertaining this family of materials are drawn.

## Theoretical Background

We briefly summarize here the main concepts employed in the TQC approach in order to develop a topological classification of the electronic bands in penta-materials. First, a direct space characterization of the states is needed. This is done in terms of real space locations given by Wyckoff positions (WPs) and atomic or Wannier orbitals. Each WP has associated a site-symmetry group (SSG), composed by the set of symmetry operations that leaves the WP invariant. The SSG is a subgroup of the complete space group of the material[12]. Assuming that there are $n_W$ orbitals at each WP, one has to identify the real-space irreducible representation with which these orbitals transform under the corresponding site-symmetry group. This gives a complete characterization of the states in real space. Next, the connection to reciprocal space is achieved via a Frobenius procedure[12], which induces the so-called band representation[36], thus giving the relationship between real and momentum description. If the WP under consideration is a maximal WP[11], it has a maximal site symmetry group associated. In this case the induced representation in reciprocal space is called an elementary band representation (EBR). The EBRs are the building blocks to describe all the groups of bands for a particular space group[12]. In order to identify the topological character of the bands, it is necessary to analyze their global connectivity in reciprocal space. By means of graph theory, all the possible connections among high-symmetry points compatible with the crystal symmetry constraints can be obtained[13,37]. This allows to classify the EBRs as connected or disconnected. Disconnected EBRs, which can be decomposed, present topological nontrivial behavior. The information about EBRs and compatibility relations for all space groups is available at the Bilbao Crystallographic server[38].

## Symmetry Analysis

Following the guidelines of the TQC approach, the fundamental starting point for the analysis of penta-materials is the knowledge of their symmetry group. The only formal requisite we impose to this class of materials is that their space group remains unaltered. Specifically, the space group of the penta-material lattice (see Fig. 1) is given by the $P\bar{4}2_1mm$ or no. 113 group[39]. Importantly, it is a nonsymmorphic group; it includes a glide plane with a fractional translation vector given by $\mathbf{t} = (a/2, a/2, 0)$, where $a$ is the lattice constant of the material. The nonsymmorphic character has direct consequences on the energy bandstructure in momentum space, as we will see below.

The topological nontrivial character of a material is directly related to the behavior of high-symmetry points (HSP) and high-symmetry lines (HSL). If a reciprocal wavevector $k$ is a HSP or belongs to a HSL, there are certain operations of the space symmetry group $G$ (modulo a reciprocal wavevector) that leaves it invariant. This set of operations form the so-called little group of $k$, $G_k$, which is a subgroup of $G$[39]. The two-dimensional BZ belonging to the space group no. 113 is presented in Fig. 2. The most relevant set of $k$ points in this group for the subsequent analysis are $\Gamma$, $X$, $M$, and the $Y$-line.

Let us begin with $\Gamma$. All the transformations of the space group leave this point invariant, so its little group is isomorphic to the space group of the system. With respect to $X$, the symmetry transformations that leave the point invariant are $I$, $2_{001}$, $\left(2_{100}|\frac{1}{2}\frac{1}{2}0\right)$. Therefore, there are three equivalence classes for $G_X$, and in principle the same number of irreps. However, using the $\sum h_l^2 = n$ constraint[40], where $h_l$ is the dimension of the $l$-th irrep and $n = 4$ is the order of the group, we obtain that only a two-dimensional irrep can exist. This irrep is labeled as $X_1$. For the $M$ point, the invariant operations are $I$, $2_{001}$, $\bar{4}^+_{001}$, $\bar{4}^-_{001}$, $\left(2_{100}|\frac{1}{2}\frac{1}{2}0\right)$, $\left(2_{010}|\frac{1}{2}\frac{1}{2}0\right)$, $\left(m_{110}|\frac{1}{2}\frac{1}{2}0\right)$ and $\left(m_{1\bar{1}0}|\frac{1}{2}\frac{1}{2}0\right)$. Thus $M$ is invariant under the complete space group $G$, so $G_M \cong G$. However, as $k \neq 0$, we have a phase of $e^{i\mathbf{k}_M\cdot\mathbf{t}}$ that is present in the wavefunction at momentum space. As $\sum h_l^2 = 8$ it follows that $h_1 = h_2 = h_3 = h_4 = 1$ and $h_5 = 2$. The character table for this little group is given in Table 1, that includes some complex characters due to the nonsymmorphic nature of the group. Finally, the symmetry transformations for the $Y$ line are $I$ and $\left(2_{010}|\frac{1}{2}\frac{1}{2}0\right)$. Since we have two classes with only one element each, there are two irreps. The corresponding character table is shown in Table 2, which also contains some complex characters.

The former data for the little groups allows for the description of the degeneracies at these HSPs and HSLs. An important remark is pertinent in this place. Namely, if the system possesses time reversal symmetry, we have to resort to use only conjugate pairs of complex-valued irreps, known as physically irreducible representations[11]. With this in mind we analyze all points listed above. The $\Gamma$ point has one- and two-dimensional real representations, thus no TRS constraint is necessary. At $X$ there is only one irrep with dimension two; therefore, this point always has a two-fold degeneracy for a spinless system. The $M$ point has four complex-valued representations and one real-valued representation. TRS forces us to combine these four irreps in two pairs of

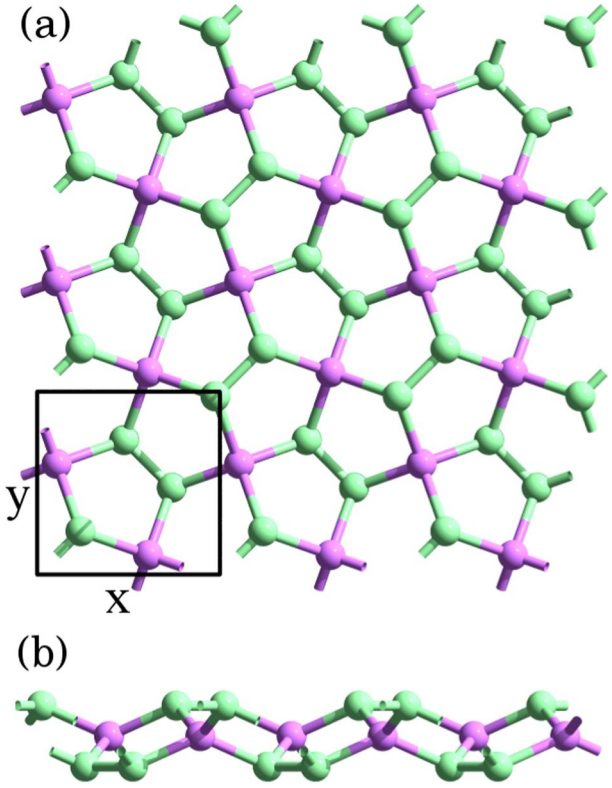


**Figure 1.** (**a**) Top and (**b**) side views of the PG lattice, after Fig. 1 of Ref.[28]. The unit cell comprising 6 atoms is enclosed in a black square.

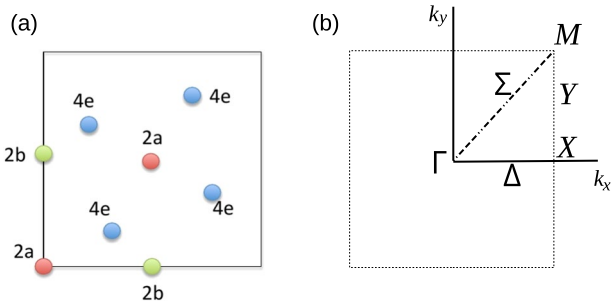


**Figure 2.** (**a**) Two-dimensional projection of the Wyckoff positions for the space group of penta-materials. (**b**) Two-dimensional Brillouin zone for penta-materials, indicating the high-symmetry points and special lines.

| M-point | $I$ | $2_{001}$ | $\bar{4}^{+}_{001}$ | $\left(2_{010}\middle\vert\frac{1}{2}\frac{1}{2}0\right)$ | $\left(m_{110}\middle\vert\frac{1}{2}\frac{1}{2}0\right)$ |
|---|---|---|---|---|---|
| $M_1$ | 1 | 1 | 1 | $i$ | $-i$ |
| $M_2$ | 1 | $-1$ | $-1$ | $-i$ | $-i$ |
| $M_3$ | 1 | $-1$ | 1 | $i$ | $-i$ |
| $M_4$ | 1 | 1 | $-1$ | $-i$ | $i$ |
| $M_5$ | 2 | 0 | 0 | 0 | 0 |

**Table 1.** Character table for $G_M$.

| Y-line | $I$ | $\left(2_{001}\middle\vert\frac{1}{2}\frac{1}{2}0\right)$ |
|---|---|---|
| $Y_1$ | 1 | $\omega$ |
| $Y_2$ | 1 | $\omega^*$ |

**Table 2.** Character table for $G_Y$. $\omega = e^{i\mathbf{k}_Y\cdot\mathbf{t}}$.

conjugate physical irreps. This process yields the pairs $M_1 + M_4$, $M_2 + M_3$ and the real $M_5$. All three physical irreps are two-dimensional. Thus, as long as TRS holds and the space group is nonsymmorphic, the energy bands at this point will be two-fold degenerate. Finally, imposing TRS at the $Y$ line we are left with only one possible physical irrep, $Y_1 + Y_2$, which is also two-dimensional. Therefore, every point located at $Y$ has a two-fold degeneracy. It is worth to notice that the $Y$ line, along with the $X$ and $M$ points, comprise all the inequivalent points at the BZ boundary. As there is a two-fold degeneracy in each case, it occurs a two-fold band touching over the entire BZ perimeter. This phenomenon is known as a nodal-line degeneracy[41].

If the spin degree of freedom is taken into account, the first trivial consequence is the doubling of the spinless original degeneracy. In this case, the trivial addition of spin yields a four-fold degeneracy along the nodal line. A more interesting scenario arises when SOC is included. Symmetry considerations must be extended to include double groups[40]. Consequently, the analysis for the little groups should be performed again, and the bands should be relabeled according to the new spinorial irreps.

Let us proceed with the analysis. The little group of the Γ point, $G_\Gamma$, is enlarged to embrace two new spinorial irreps labeled by $\overline{\Gamma}_6$ and $\overline{\Gamma}_7$; see Supplementary Material (SM) for the character table of this particular group and all the double groups used in this work. These two irreps are two-dimensional, which implies that the maximal degeneracy at this point is two. As commented above, the $X$ point is described by a unique two-dimensional irrep without spin; the inclusion of SOC enlarges the character table. This can be easily seen using the basic relation $\sum h_l^2 = 6$, where the solution is given by $h_1 = 2$ and $h_2 = h_3 = h_4 = h_5 = 1$. Thus, four new one-dimensional complex representations are added with respect to the spinless case. If TRS holds, these irreps are joined in conjugate pairs, giving two possible physical irreps, namely, $\overline{X}_2 + \overline{X}_4$ and $\overline{X}_3 + \overline{X}_5$, both two-dimensional. This last result implies that degeneracy is lifted, as in the Γ point, splitting the group of four bands into two pairs of bands.

The double group for the $Y$ line has two more, complex and one-dimensional irreps: $\overline{Y}_3$ and $\overline{Y}_4$ (see SM). Like in the previous cases, TRS implies the pairing of both irreps in the physical irrep $\overline{Y}_3 + \overline{Y}_4$, forming a two-dimensional irrep. Therefore, as in Γ and $X$, the possible four-fold degeneracy is lifted, yielding two stick-together, two-fold degenerate bands, along the whole line. Finally for the $M$ point, the double group includes now two new spinorial irreps $\overline{M}_6$ and $\overline{M}_7$, both two-dimensional and complex-valued irreps (see SM). Under TRS these two irreps have to be paired in a single physical irrep, denoted as $\overline{M}_6 + \overline{M}_7$. This irrep is four-dimensional; being the only option for the spinful case, we conclude that the $M$ point is unaffected by the inclusion of SOC, maintaining the four-fold degeneracy for the energy bands. In summary, we have shown, based only on symmetry grounds, that the boundary nodal line disappears under SOC, leaving only a point-like degeneracy at $M$.

We finish the exploration of symmetries in penta-materials by relaxing time-reversal invariance. If TRS is broken, single complex irreps can be physical representations without the need of coupling them in conjugate pairs. This has straightforward implications in the degeneracy landscape of the energy bands, with or without SOC. If TRS is absent and no SOC is considered, the following consequences can be deduced: (i) The Γ point is still four-fold degenerated; (ii) The $X$ point becomes non-degenerate; (iii) The $M$ point changes its degeneracy from four-fold to two-fold; and finally, (iv) at the $Y$ line we find non-degenerate bands, implying the disappearance of the nodal line for this case.

Additionally, in the SOC plus TRS breaking case we can deduce the following: (i) at Γ nothing happens, since all irreps are already real; however, (ii) the conjugate pairs formed at $X$ under TRS break apart in the single complex one-dimensional irreps $\overline{X}_2$, $\overline{X}_4$, $\overline{X}_3$, $\overline{X}_5$. Therefore, all bands are non-degenerate at this point. The $M$ point, which had a protected four-fold degeneracy, due to time-reversal and nonsymmorphic symmetries, ends up with a pair of two-fold degenerated bands. Finally, the degeneracy of the $Y$ line is lifted, leaving four non-degenerate bands for each group of the eight bands occurring in the spinful model.

## Topological Analysis

In order to apply the topological analysis based on the symmetry description given in the previous section, we need to establish a model for the relevant energy range, namely, the vicinity of the Fermi level. All the penta-materials presented here have the pentagonal lattice of PG as a basic structure (Fig. 1), which has six atoms in its unit cell, four of them with coordination 3 and the other two with coordination 4. In terms of Wyckoff positions (WPs), the atoms with coordination 3 are located at a non-maximal 4e WP, and those with coordination 4 are allocated at a maximal 2a WP. Figure 2 presents a graphical description of WPs for this particular space group.

With the WPs of the atoms identified, the real space description is completed enumerating the orbital components for each atomic site. The most important contribution for the considered penta-materials comes from the $p_z$ orbitals, and in particular from atoms at the 4e WP. We present a minimal model for the topological analysis based on the four $p_z$ orbitals at the 4e WP. Extensions to this model including additional atoms, either adsorbed or as substitutions, can be also important and may involve other combinations of atomic orbitals. However, in terms of the essential topological behavior the main results are not modified, so we rely on this minimal model and discuss the necessary additions when appropriate.

Once the real space model is complete, it has to be translated to momentum space, with the aim to compute its induced band representation and the subsequent topological characteristics. To calculate the corresponding band representation, the site-symmetry group (SSG) related to the 4e WP[12] should be identified. This group is composed of two operations, $I$, and $2_{001}$. Its character table is given in Table 3 (we are only considering the first two columns and rows in this table for the single-valued SSG). In a first stage we ignore spin-orbit coupling and assume that TRS holds, which implies the use of physical irreducible representations[11]. The $p_z$ orbitals transform as the $A'$ irrep of this SSG. This information allows to define an induced band representation which gives as a result the symmetry (irrep labels) of the four bands throughout the entire BZ, as shown in Table 4. Here we only show explicitly the TR-symmetric points Γ, $X$ and $M$.

| 4e | $I$ | $2_{001}$ | $I^d$ | $2^d_{001}$ |
|---|---|---|---|---|
| $A'$ | 1 | 1 | 1 | 1 |
| $A'$ | 1 | $-1$ | 1 | $-1$ |
| $\overline{E}_1$ | 1 | $-i$ | $-1$ | $i$ |
| $\overline{E}_2$ | 1 | $i$ | $-1$ | $-i$ |

**Table 3.** Character table for the double site-symmetry group at 4e Wyckoff position.

| B Zpoint | $A' \uparrow G$ |
|---|---|
| $\Gamma$ | $\Gamma_1(1) \oplus \Gamma_3(1) \oplus \Gamma_5(2)$ |
| $X$ | $2X_1(2)$ |
| $M$ | $M_1(1)M_3(1) \oplus M_5(2)$ |

**Table 4.** Band representation for 4*e* WP with TRS and no SOC.

| B Zpoint | $\overline{E}_1 + \overline{E}_2 \uparrow G$ |
|---|---|
| $\Gamma$ | $2\overline{\Gamma}_6(2) \oplus 2\overline{\Gamma}_7(2)$ |
| $X$ | $2\overline{X}_2\overline{X}_5(2) \oplus 2\overline{X}_3\overline{X}_4(2)$ |
| $M$ | $2\overline{M}_6\,\overline{M}_7(4)$ |

**Table 5.** Band representation for 4*e* WP, with SOC and TRS.

| B Zpoint | $2\overline{E}_1 \uparrow G$ |
|---|---|
| $\Gamma$ | $2\overline{\Gamma}_6(2) \oplus 2\overline{\Gamma}_7(2)$ |
| $X$ | $2\overline{X}_2(1) \oplus 2\overline{X}_5(1) \oplus 2\overline{X}_3(1) \oplus 2\overline{X}_4(1)$ |
| $M$ | $2\overline{M}_6(2) \oplus 2\overline{M}_7(2)$ |

**Table 6.** Band representation for 4*e* WP with SOC and no TR.

A straightforward observation is that this band representation is composite[11]. This is to be expected, since our model is based on $p_z$ orbitals located at non-maximal WP. Nevertheless, we can express this band representation as a sum of EBRs coming from maximal WP: $A' \uparrow G = (2a) \uparrow G \oplus (2c) \uparrow G$ (see[38] for the complete list of EBRs for the group). The most important conclusion for this model is that all sets of bands are two-connected, and therefore all bands are topologically trivial. Particular examples of this phase show some variations of the electronic character of the material, depending on the specific band filling. The inclusion of SOC can lead to the appearance of additional phases in these materials. This implies the use of a double group (double SSG) description, as mentioned before. The character table for the corresponding double group is given in Table 3. Due to TRS, we have to apply the conjugate pair procedure and join the $\overline{E}_1$ and $\overline{E}_2$ irreps in a single $\overline{E}_1 + \overline{E}_2$ physical irrep for the spinful orbitals. This two-dimensional irrep induces a band representation in reciprocal space shown in Table 5.

The above band representation takes into account eight bands arising from the spin degree of freedom. Additionally, by exploring the character of all the EBRs with TRS for this double group, it can be verified that all sets of bands are connected, with a maximum of 4-connected bands (see[38]). Thus, all bands are trivial in this case. Still, we have some SOC-induced transitions at the HSPs and HSLs that modify the degeneracy order as mentioned in the symmetry analysis, this has consequences on the electronic properties of particular penta-materials (see next Section).

Finally, we consider TRS breaking such that complex-valued irreps are allowed. With the same induction procedure employed above, we found the band representation shown in Table 6.

This is a composite band representation formed by two groups of four bands. We study only one group, since the other one has exactly the same structure.

As it is well-known, degeneracy is lowered by TRS breaking and, this is reflected in the band representation which becomes decomposable, a signal for the presence of a topological set of bands[11–13]. If an EBR is decomposable, then different connectivity paths can appear among the high symmetry points and lines through the BZ, which implies different topological phases in the material. The different topological realizations of the band representation correspond to all possible solutions of the compatibility relations between HSPs and HSLs over the BZ. We have carried this process for a two-dimensional BZ of the space group of penta-materials, finding the connectivity solutions presented in Table 7 below.

These sets of bands have to be compared with the EBRs that the space group induces in momentum space. As a general rule, if a band representation can be expressed as the combination of some EBRs, then the set of bands

| HSP path | Character |
|---|---|
| $\Gamma_6 \to X_2 \oplus X_4 \to M_6$ | trivial |
| $\Gamma_7 \to X_3 \oplus X_5 \to M_7$ | topological |
| $\Gamma_6 \to X_3 \oplus X_5 \to M_6$ | topological |
| $\Gamma_7 \to X_2 \oplus X_4 \to M_7$ | trivial |
| $\Gamma_7 \to X_2 \oplus X_4 \to M_6$ | topological |
| $\Gamma_6 \to X_3 \oplus X_5 \to M_7$ | trivial |
| $\Gamma_7 \to X_3 \oplus X_5 \to M_6$ | trivial |
| $\Gamma_6 \to X_2 \oplus X_4 \to M_7$ | topological |

**Table 7.** Compatibility relations along different high-symmetry-point paths of these family of penta-materials, allowing for the determination of their topological and trivial phases.

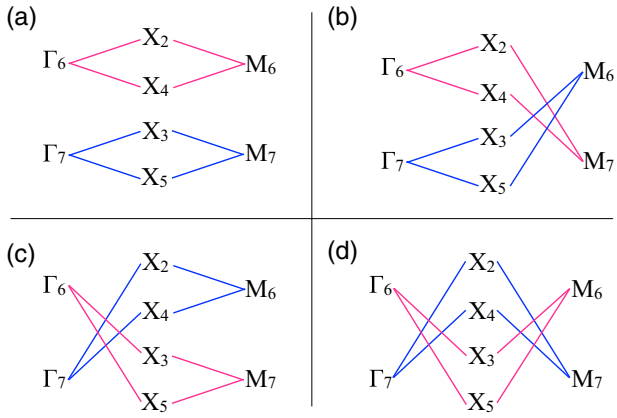


**Figure 3.** Scheme of the possible energy orderings of bands (irreps) at the high-symmetry points and high-symmetry lines.

is trivial[12]. Comparing the results for the band representations above with all possible EBRs, it can be seen that some sets cannot be expressed in terms of EBRs; in conclusion, such bands are topological. The labeling presented in the Table 7 depicts this situation.

There are four different possible connectivities that depend on the particular characteristics and band filling of the material. We can build a toy model to grasp the general behavior of these phases by fixing the energy ordering of bands (irreps) to some particular sequence at HSPs and HSLs. The possible outcomes are depicted graphically in Fig. 3. There are three phases presenting nodal degeneracy and one phase with gapped character. The knowledge of the specific band filling is necessary in order to classify this topological behavior as metallic or insulating. This is strongly material-dependent, making it necessary to analyze specific cases. In particular, for penta-materials studied in this work, there is an interplay of metallic phases with or without nodes, along with electron or hole pockets near the Fermi energy, an scenario that has been found before[42]. In summary, if TRS is preserved and no SOC is included, penta-materials possess a general band structure with trivial bands in all its energy range, displaying a perimeter nodal line. The inclusion of SOC while maintaining TRS yields also trivial bands, but some degeneracies are lifted in the BZ, changing the character of the electronic properties. Breaking TRS with SOC produces a decomposable band representation that gives rise to four different topological phases, according to the distinct possibilities for the band connectivity.

This exhausts our study of the electronic band structure for penta-materials within a general group theory framework. Naturally, other perturbations could be included in order to modify the symmetry character of the underlying lattice with the possible induction of more topological phases.

In the following section we apply this general group-theoretical description to some specific penta-materials. This is done with the aid of first-principles calculations and effective models.

## Examples of Penta-Materials

The first instance of this family of materials is penta-graphene. It has an all-carbon lattice structure and an insulating character. Two conduction bands and two valence bands are the main contributors to the low-energy range[15]. Applying the TQC analysis it can be concluded that, since carbon has a weak SOC and TRS holds, PG is a trivial (band) insulator. In this context, PG presents little interest due to its sizeable optical gap. However, as mentioned before, we can explore additional configurations by functionalization, adsorption or atom substitution of penta-graphene without altering its original symmetry. This can be reinforced by an electron filling analysis as presented in[43]. For the PG space group (No. 113) the band insulator filling is dictated by a $4n$ relation, where $n$ is a positive integer. For PG this yields a band filling of 36, which results in a band insulator state. If we substitute some carbon atoms we deviate from the $4n$-band filling, accomplishing a condition for the filling-enforced

| System | $a$(Å) | $cc$(Å) | $cx$(Å) | $d$(Å) |
|---|---|---|---|---|
| PG | 3.650 | 1.554 | | |
| $NC_2$ | 3.417 | 1.403 | 1.516 | |
| $PC_2$ | 4.178 | 1.418 | 1.815 | |
| $BC_2$ | 4.017 | 1.388 | 1.647 | |
| $MnC_2$ | 4.630 | 1.262 | 2.183 | |
| Li-PG | 3.695 | 1.576 | | 2.188 |
| Na-PG | 3.790 | 1.602 | | 2.564 |

**Table 8.** Lattice constants and relevant atomic distances of the penta-materials studied in this work. Here $a$ is the lattice constant, $cc$ the carbon-carbon distance, $cx$ the distance between a carbon atom and the other element X and $d$ is the distance between the carbon atom and the absorbed Li or Na.

formation of a nodal (semi)metal. This has to be additionally cross-checked with a chemical stability study of the material[44].

We present first-principles calculations for several penta-materials based on PG, with an emphasis in both, global and local features of their energy bands. We explain the modifications performed in PG to achieve the specific penta-material and the particular phase realizations with respect to our previous symmetry and topological analysis.

Our calculations were carried out in the density functional theory (DFT) framework using SIESTA[45] and Quantum ESPRESSO[46,47] *ab initio* packages. The energy cutoff for the basis set was 80 Ry for Quantum ESPRESSO and for SIESTA calculations we employed localized atomic orbitals as a basis set (double-$\zeta$, single polarized). In both codes were employed norm-conserving pseudopotentials and the structures were relaxed until the forces on the atoms were less than 0.04 eV/Å. Exchange-correlation was considered within the generalized gradient approximation (GGA), as proposed by Perdew, Burke, and Ernzerhof[48]. The convergence of the total energy is ensured with a Monkhorst-Pack k-grid of $15 \times 15 \times 1$ in both cases. All the geometrical parameters for the penta-materials presented below were obtained from SIESTA code and are summarized in Table 8. Calculations of materials without spin-orbit coupling were carried out with SIESTA and Quantum ESPRESSO giving similar results. Calculations including spin-orbit coupling were performed exclusively with Quantum ESPRESSO.

## Symmetry-Protected Metallic Phases

In order to access the metallic phases, i.e., to shift the conduction or valence bands, other elements rather than carbon should be added to PG. We first functionalize PG with adsorption of metallic atoms at 4e WP. This case has been previously explored for various elements, showing metallization of PG[32,33]. An example of a relaxed lattice structure with adsorbed Li is presented in Fig. 4. Also, electronic band structure calculations are shown for this case of Li-adsorbed PG (Li-PG) as well as Na-adsorbed PG (Na-PG) in Fig. 5. Another possibility is to explore substitutional derivatives of PG, respecting the original symmetry. Particularly interesting for this work is the 2a WP, which corresponds to coordination-4 atoms, forming a penta-$XC_2$ configuration[31,34,35], where X = {B, N, P, Si, Ge}. The lattice structure of these materials is exactly the same as PG, with modifications in the relative bond magnitudes and lattice constant. We show the band structures for X = B, N, P in Fig. 6.

Since these theoretical materials preserve the PG space group $P\bar{4}2_1mm$, they show a similar trend in the electronic band structure. However, now there is a fractional filling of the conduction (valence) band, which can be described in this trivial phase (no SOC + TRS) by a single EBR. As stated by Bradlyn *et al.*[11], if the Fermi level sits on a single EBR with fractional filling, the corresponding material is necessarily a protected (semi)metal. Thus, all these metal-PG and penta-$XC_2$ materials are symmetry-protected metals. We have some remarks about this result. The above-mentioned symmetry protection is of crystalline character; since the space group is nonsymmorphic and TRS symmetry is preserved, it implies the well-known "stick-together" phenomenon for energy bands[40] along the $Y$ line. This effect can be seen in the band structures of all penta-materials in this regime. It is remarkable that the sticky bands occur along all the BZ boundary. Consequently, there is a trivial crystalline nodal line for these penta-materials. The nodal line presents a certain dispersion, i.e., it is not at constant energy in momentum space. Such dispersion can be due to several causes; for example, breaking particle-hole, chiral and/or crystalline symmetries. The lack of inversion symmetry has been invoked in previous works as the reason for the dispersion of these lines[41,42]. However, planar pentagonal materials, for which inversion symmetry holds[49], also have a certain dispersion in the $Y$ line; therefore, particle-hole and chiral symmetry breaking play an important role in this effect[50].

For PG-adsorbed or substituted materials, although the nodal line is energy-dependent, it crosses the Fermi energy, producing a single nodal point plus pockets of electrons or holes. This can be clearly seen in the band structures shown in Figs 5 and 6. Looking closer to the local low-energy behavior of the nodal line at the vicinity of the $Y$ line, we observe that bands have a linear dependence on $k_x$ along constant $k_y$ lines, so these carriers behave as massless fermions. This can be observed in a momentum space cut presented in Fig. 7. We can see that the node line is composed by a succession of Dirac nodes, with the Dirac point sitting at the $Y$ line. The massless fermion low-energy dispersion becomes more relevant if the Fermi level actually sits on a state of the nodal line. This crucially depends on the band filling fraction, being realizable in some of the materials studied. Notice that, although we have a trivial phase in these materials, we still can have protected edge states. This can be explained in terms of the ten-fold way classification of the Fermi surface[51]. As the considered materials belong to the AIII (chiral unitary) class, for spatial dimension $d = 2$ a trivial phase arises, as expected. But due to an

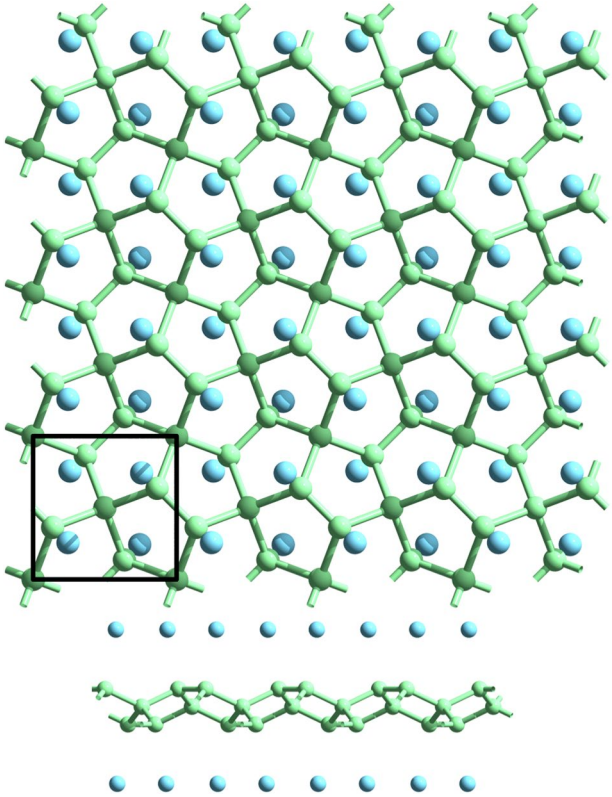

**Figure 4.** Relaxed lattice of penta-graphene (green) with adsorbed Li atoms (cyan).

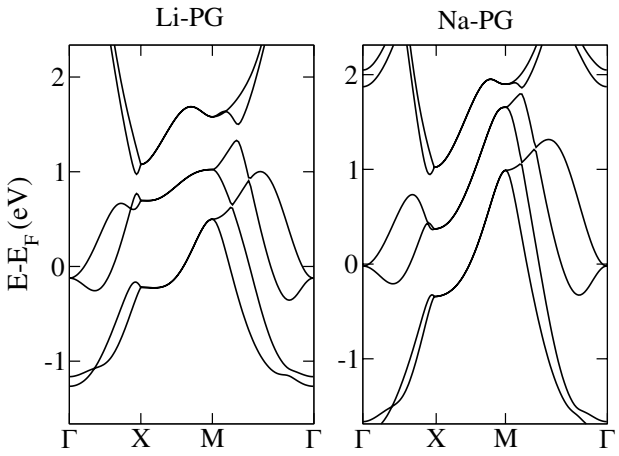


**Figure 5.** Band structures of Li (left panel) and Na (right panel) absorbed on penta-graphene along the special symmetry lines.

inherited non-triviality from another related AI (orthogonal) class, robust edge states that present linear or dispersionless characteristics might appear[9]. Next, SOC effects are explored by means of first-principles calculations. To this end, we use as an example penta-$PC_2$. Its band structure is presented in Fig. 8. As we are dealing with light elements the effect of SOC is rather weak; therefore, all these materials will behave as nodal line semimetals at room temperature, showing a continuum of Dirac nodes along the Brillouin zone boundary. Furthermore, these Dirac points are accessible under variations of the Fermi level position, making these massless fermions available under different perturbations, such as doping or electrostatic gating.

Notwithstanding, the results derived by the symmetry analysis are confirmed. Namely, degeneracies at Γ and *X* points and along the *Y* line are lifted. Likewise, the robustness of the *M* point four-fold degeneracy is confirmed by these calculations, which allows us to identify this as a novel metallic phase similar to that studied by Topp *et al.*[52]. The symmetry that protects the "stick-together" effect along the *Y* line is broken, and the

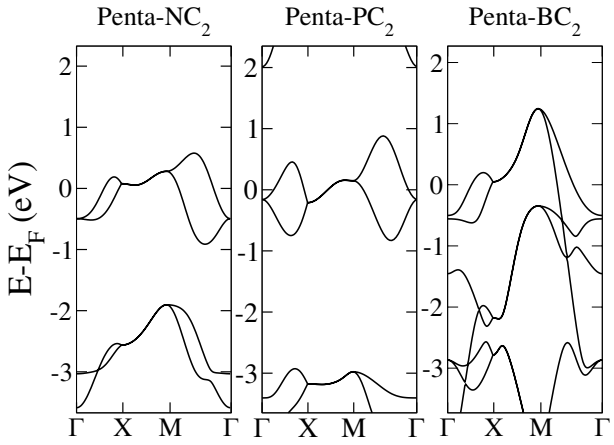


**Figure 6.** Band structures of different $XC_2$ penta-materials. Left panel: penta-$NC_2$; central panel: penta-$PC_2$; right panel: penta-$BC_2$.

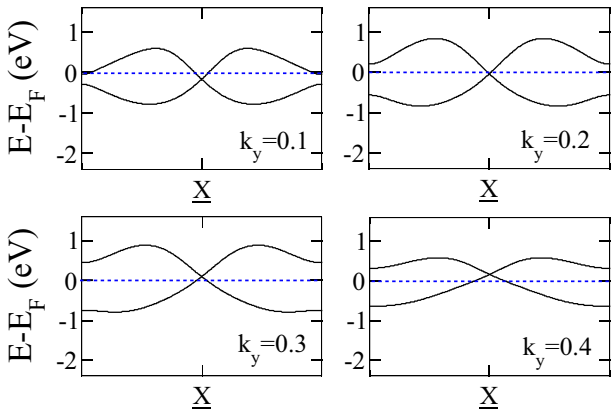


**Figure 7.** Penta-$NC_2$ band structure along several lines perpendicular to Y given by fixed $k_y = 0.1, 0.2, 0.3, 0.4$ values. X denotes the point at Y, for which a Dirac node is evident.

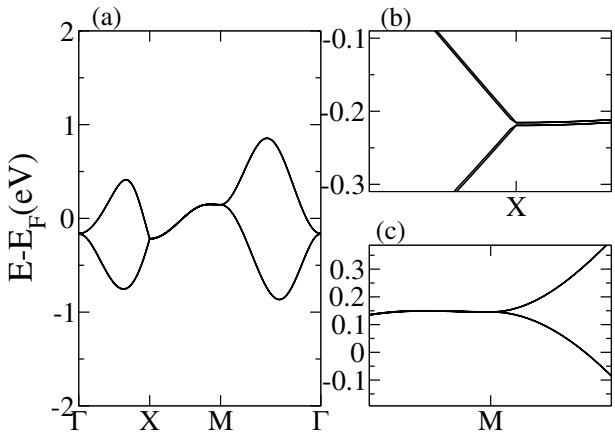


**Figure 8.** Penta-$PC_2$ band structure with SOC. (**a**) Detail of the bands around the Fermi energy. (**b**) Zoom of the bands at the M point, where the SOC splitting can be distinguished. (**c**) Zoom around the M point, showing that the bands remain degenerate at this point.

degeneracy of the above-mentioned high-symmetry points is also modified, implying the disappearance of the nodal line. Therefore, for these penta-materials, SOC plus TRS enforces a transition from a nodal line metal state to a spin-orbit Dirac-node metal with nodal points located at $M$[53,54], both phases being topologically trivial.

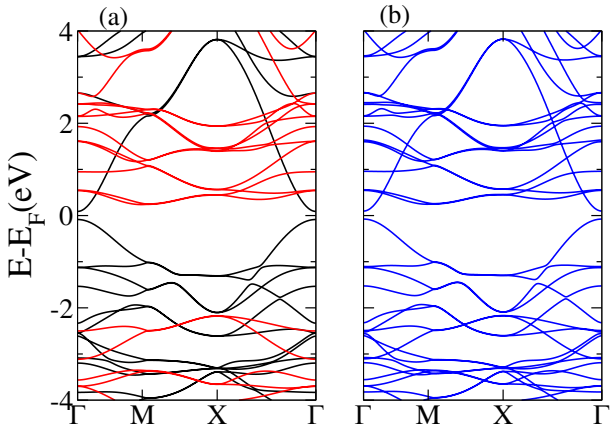


**Figure 9.** DFT penta-$MnC_2$ band structures (**a**) without SOC; black and red denote spin-up and spin-down bands, respectively. (**b**) Bands including SOC.

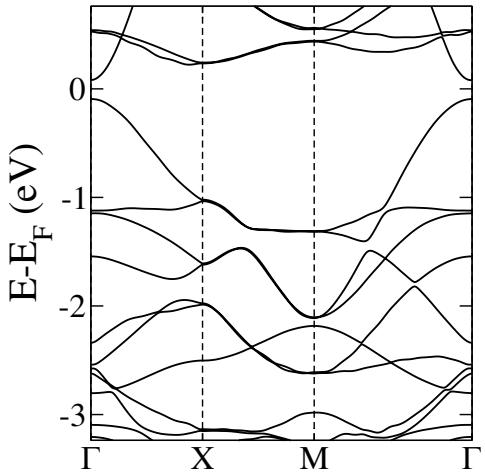


**Figure 10.** Penta-$MnC_2$ band structure calculated with the Wannier function basis.

## Topological phase: Breaking TRS

In what follows we show an example of a penta-material for the TRS-breaking phase with SOC: PG with substitution of Mn atoms at the 4e WP (or penta-$MnC_2$). In this case, magnetic Mn atoms break TRS and induce an intrinsic spin-orbit interaction, which results in a nontrivial phase. The corresponding band structure calculations are presented in Fig. 9. In this example the four-fold to two-fold change of degeneracy at the *M* point due to TRS breaking can be corroborated. We observe that along this high-symmetry path no band crossing among the four-band subgroups occurs. Further, the *Y* line is completely non-degenerate, as expected. Thus, we have a situation similar to the "*a*" phase presented in the model introduced in the Section "Topological analysis". We also find that the structure is magnetic and choose a ferromagnetic configuration, which is energetically more favorable. We ignore further magnetic group information for the subsequent analysis and restrict only to double space group data.

In the case of nontrivial phases it is also necessary to establish a topological classification based on the calculation of topological invariants. In this case, we will use a numerical technique known as Wannier Charge Center (WCC) evolution[55,56]. In order to implement this procedure, an effective model defined in terms of Wannier functions must be supplied. We construct this model for the low-energy regime of penta-$MnC_2$ using the code Wannier90[57,58]. This code uses a DFT band structure calculation as the input and wannierize the system by projecting the eigenfunction space to an initial set of orbitals. We chose $sp^3$ orbitals for C atoms plus *s* and *d* orbitals for Mn atoms. This is an extension of the basic model with only *s* and *p* orbitals; in this case the *d* orbitals transform as the *p* orbitals for the SSG of the 4e WP. We set a tolerance of $10^{-10}$ for the wannierization (minimization) procedure and define a frozen energy window of 3 eV around the Fermi level taking into account 20 bands. With this model at hand, the band structure of penta-$MnC_2$ can be computed; it is shown in Fig. 10. It shows a very good agreement with that obtained from first-principles methods, being a good starting model for the calculation of topological invariants.

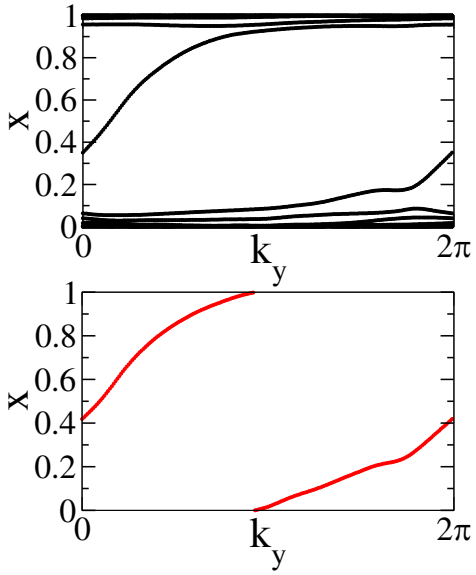


**Figure 11.** Top: WCC evolution for *x* axis. Bottom: Sum of WCC for the *x* axis.

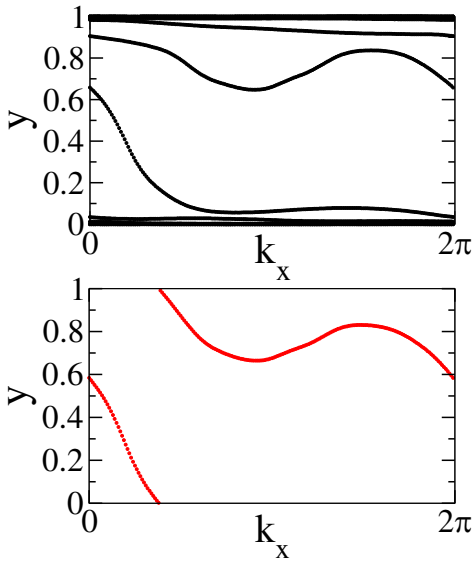


**Figure 12.** Top: WCC evolution for *y* axis. Bottom: Sum of WCC for the *y* axis.

The WCC evolution is related to several topological invariants such as $\mathbb{Z}_2$ and Chern numbers. In the particular case we are studying, since TRS is broken[5] we compute the so-called individual Chern numbers[59]. They can be used to classify crystalline symmetries, as mirror or spatial inversion. In the case of TRS systems, these numbers give rise to a $\mathbb{Z}$ classification of phases, and can be added to obtain the net Chern number. For 2D magnetic materials, with broken TRS, each individual Chern number has to be taken separately, providing a $\mathbb{Z} \times \mathbb{Z}$ classification with ($C_x$, $C_y$) topological numbers. The individual Chern numbers are obtained by taking the sum of the WCCs at each $k$ point and then counting the times this function winds across the vertical axis over the entire $k$-path[55]. This procedure has the advantage that only bulk properties are needed to compute the topological invariants of a material, without resorting to more expensive surface or edge state calculations. To this purpose, we have used two codes: Z2pack[60] and WannierTools[61]. Only the Z2pack results are presented here, since WannierTools gives a similar outcome. Z2pack uses the Hamiltonian in terms of Wannier functions as an input. Additionally, we set a position tolerance of 0.001, a gap tolerance equal to 0.1 eV and a number of lines of 200. The WCC calculation can be carried for each one of the spatial directions of the system. For penta-materials, being 2D systems, there are two directions, $x$ and $y$. We present the WCC evolution and WCC sum for both directions in Figs 11 and 12, respectively.

It can be observed that the individual Chern numbers are non-zero for both directions. In particular, a Chern number of $C_x = 1$ was obtained for the $x$-direction and $C_y = -1$ for the $y$-direction, related to the winding of the

sum of the WCC across the respective $k$ directions. This implies a charge pumping effect along each $k$-space direction[56] and hints for a nontrivial topological phase at the bulk gap. The former discussion gives a total chern number of $C = 1$, as $C = C_x = -C_y = 1$ [60] and therefore, we conclude that penta-$MnC_2$ is a material realization for a chern insulator phase.

## Conclusions

We have studied a set of materials sharing a space group structure that we dub penta-materials. A detailed analysis for many physical possibilities, including TRS and TRS breaking as well as SOC, shows that these materials can host different phases. We have found nodal line fermions if SOC is weak and TRS is present; in metallic penta-materials this implies that a continuum of Dirac points is accessible around the Fermi energy. Also, symmetry-protected Dirac points arise if SOC is strong enough. Finally, if TRS is broken and SOC is sufficiently strong, we encounter a nontrivial topological phase characterized by non-zero individual Chern numbers for the two primitive directions in $k$-space. A wider class of penta-materials, from other substitutions or functionalization, awaits for the full characterization of their topological phases and the obtention of additional physical properties.

## Data Availability

All data generated or analyzed during this study are included in this published article.

## References


1. Tse, W.-K. Magneto-optical effects in topological insulators. In Drouhin, H.-J., Wegrowe, J.-E. & Razeghi, M. (eds) *Proc. SPIE 9931, Spintronics IX*, vol. 9931, 99313I (International Society for Optics and Photonics, 2016).
2. Tse, W. K. & MacDonald, A. H. Giant magneto-optical Kerr effect and universal Faraday effect in thin-film topological insulators. *Phys. Rev. Lett.* **105**, 057401 (2010).
3. Bauer, S. & Bobisch, C. A. Nanoscale electron transport at the surface of a topological insulator. *Nature Communications* **7**, 11381 (2016).
4. Wang, S., Lin, B.-C., Wang, A.-Q., Yu, D.-P. & Liao, Z.-M. Quantum transport in dirac and weyl semimetals: a review. *Advances in Physics: X* **2**, 518–544 (2017).
5. Bernevig, B. A., Hughes, T. L. & Zhang, S.-C. Quantum spin Hall effect and topological phase transition in HgTe quantum wells. *Science* **314**, 1757–61, https://doi.org/10.1126/science.1133734 (2006).
6. Hasan, M. Z. & Kane, C. L. Colloquium: Topological insulators. *Reviews of Modern Physics* **82**, 3045–3067 (2010).
7. Bansil, A., Lin, H. & Das, T. Colloquium: Topological band theory. *Reviews of Modern Physics* **88**, 021004, https://doi.org/10.1103/RevModPhys.88.021004 (2016).
8. Slager, R.-J., Mesaros, A., Juričić, V. & Zaanen, J. The space group classification of topological band-insulators. *Nature Physics* **9**, 98, https://doi.org/10.1038/nphys2513 (2012).
9. Chiu, C.-K., Teo, J. C. Y., Schnyder, A. P. & Ryu, S. Classification of topological quantum matter with symmetries. *Rev. Mod. Phys.* **88**, 035005, https://doi.org/10.1103/RevModPhys.88.035005 (2016).
10. Kruthoff, J., de Boer, J., van Wezel, J., Kane, C. L. & Slager, R.-J. Topological classification of crystalline insulators through band structure combinatorics. *Phys. Rev. X* **7**, 041069, https://doi.org/10.1103/PhysRevX.7.041069 (2017).
11. Bradlyn, B. *et al.* Topological quantum chemistry. *Nature* **547**, 298–305 (2017).
12. Cano, J. *et al.* Building blocks of topological quantum chemistry: Elementary band representations. *Phys. Rev. B* **97**, 035139 (2018).
13. Bradlyn, B. *et al.* Band connectivity for topological quantum chemistry: Band structures as a graph theory problem. *Phys. Rev. B* **97**, 035138 (2018).
14. Tang, C.-P., Xiong, S.-J., Shi, W.-J. & Cao, J. Two-dimensional pentagonal crystals and possible spin-polarized dirac dispersion relations. *Journal of Applied Physics* **115**, 113702, https://doi.org/10.1063/1.4868679 (2014).
15. Zhang, S. *et al.* Penta-graphene: A new carbon allotrope. *Proc. Natl. Acad. Sci. USA* **112**, 2372–2377 (2015).
16. Zhang, C., Zhang, S. & Wang, Q. Bonding-restricted structure search for novel 2d materials with dispersed c2 dimers. *Scientific Reports* **6**, 29531, https://doi.org/10.1038/srep29531 (2016).
17. Liu, Z. *et al.* Penta-pt2n4: an ideal two-dimensional material for nanoelectronics. *Nanoscale* **10**, 16169–16177, https://doi.org/10.1039/C8NR05561K (2018).
18. Zhuang, H. L. From pentagonal geometries to two-dimensional materials. *Computational Materials Science* **159**, 448–453, https://doi.org/10.1016/j.commatsci.2018.12.041 (2019).
19. Zhao, K., Li, X., Wang, S. & Wang, Q. 2d planar penta-mn2 (m = pd, pt) sheets identified through structure search. *Phys. Chem. Chem. Phys.* **21**, 246–251, https://doi.org/10.1039/C8CP04851G (2019).
20. Cerdá, J. I. *et al.* Unveiling the pentagonal nature of perfectly aligned single-and double-strand si nano-ribbons on ag(110). *Nature Communications* **7**, 13076, https://doi.org/10.1038/ncomms13076 (2016).
21. Oyedele, A. D. *et al.* Pdse2: Pentagonal two-dimensional layers with high air stability for electronics. *Journal of the American Chemical Society* **139**, 14090–14097, https://doi.org/10.1021/jacs.7b04865 (2017).
22. Liu, H., Qin, G., Lin, Y. & Hu, M. Disparate strain dependent thermal conductivity of two-dimensional penta-structures. *Nano Letters* **16**, 3831–3842 (2016).
23. Yuan, P. F., Zhang, Z. H., Fan, Z. Q. & Qiu, M. Electronic structure and magnetic properties of penta-graphene nanoribbons. *Phys. Chem. Chem. Phys.* **19**, 9528–9536 (2017).
24. He, C., Wang, X. F. & Zhang, W. X. Coupling effects of the electric field and bending on the electronic and magnetic properties of penta-graphene nanoribbons. *Phys. Chem. Chem. Phys.* **19**, 18426–18433 (2017).
25. Rajbanshi, B., Sarkar, S., Mandal, B. & Sarkar, P. Energetic and electronic structure of penta-graphene nanoribbons. *Carbon* **100**, 118–125 (2016).
26. Chen, M., Zhan, H., Zhu, Y., Wu, H. & Gu, Y. Mechanical properties of penta-graphene nanotubes. *The Journal of Physical Chemistry C* **121**, 9642–9647 (2017).
27. Krishnan, R., Su, W.-S. & Chen, H.-T. A new carbon allotrope: Penta-graphene as a metal-free catalyst for CO oxidation. *Carbon* **114**, 465–472 (2017).
28. Bravo, S., Correa, J., Chico, L. & Pacheco, M. Tight-binding model for opto-electronic properties of penta-graphene nanostructures. *Scientific Reports* **8**, 11070, https://doi.org/10.1038/s41598-018-29288-8 (2018).
29. Wu, X. *et al.* Hydrogenation of penta-graphene leads to unexpected large improvement in thermal conductivity. *Nano Letters* **16**, 3925–3935 (2016).
30. Li, X. *et al.* Tuning the electronic and mechanical properties of penta-graphene via hydrogenation and fluorination. *Phys. Chem. Chem. Phys.* **18**, 14191–14197 (2016).
31. Quijano-Briones, J. J., Fernandez-Escamilla, H. N. & Tlahuice-Flores, A. Doped penta-graphene and hydrogenation of its related structures: a structural and electronic DFT-D study. *Phys. Chem. Chem. Phys.* **18**, 15505–15509 (2016).

32. Enriquez, J. I. G. & Villagracia, A. R. C. Hydrogen adsorption on pristine, defected, and 3d-block transition metal-doped penta-graphene. *International Journal of Hydrogen Energy* **41**, 12157–12166 (2016).
33. Xiao, B., Li, Y.-c, Yu, X.-f. & Cheng, J.-b. Penta-graphene: A Promising Anode Material as the Li/Na-Ion Battery with Both Extremely High Theoretical Capacity and Fast Charge/Discharge Rate. *ACS Applied Materials & Interfaces* **8**, 35342–35352 (2016).
34. Berdiyorov, G. R. & Madjet, M. E.-A. First-principles study of electronic transport and optical properties of penta-graphene, penta-SiC2 and penta-CN2. *RSC Adv.* **6**, 50867–50873 (2016).
35. Berdiyorov, G., Dixit, G. & Madjet, M. Band gap engineering in penta-graphene by substitutional doping: First-principles calculations. *J. Phys. Condens. Matter* **28**, 475001 (2016).
36. Zak, J. Band representations of space groups. *Phys. Rev. B* **26**, 3010–3023 (1982).
37. Vergniory, M. G. *et al*. Graph theory data for topological quantum chemistry. *Phys. Rev. E* **96**, 023310 (2017).
38. http://www.cryst.ehu.es/. (Bilbao Crystallographic Server, University of the Basque Country, Bilbao, Basque Country, Spain).
39. Miller, S. C. & Love, W. H. *Tables of Irreducible Representations of Space Groups and Co-Representations of Magnetic Space Groups* (Pruett Press, Denver, 1967).
40. Dresselhaus, M. S., Dresselhaus, G. & Jorio, A. *Group Theory - Applications to the Physics of Condensed Matter* (Springer, Berlin, 2008).
41. Young, S. M. & Kane, C. L. Dirac semimetals in two dimensions. *Phys. Rev. Lett.* **115**, 126803 (2015).
42. Burkov, A. A., Hook, M. D. & Balents, L. Topological nodal semimetals. *Phys. Rev. B* **84**, 235126 (2011).
43. Watanabe, H., Po, H. C., Zaletel, M. P. & Vishwanath, A. Filling-Enforced Gaplessness in Band Structures of the 230 Space Groups. *Phys. Rev. Lett.* **117**, 096404, https://doi.org/10.1103/PhysRevLett.117.096404 (2016).
44. Chen, R., Po, H. C., Neaton, J. B. & Vishwanath, A. Topological materials discovery using electron filling constraints. *Nature Physics* **14**, 55–61 (2018).
45. Soler, J. M. *et al*. The siesta method for ab initio order-n materials simulation. *Journal of Physics: Condensed Matter* **14**, 2745 (2002).
46. Giannozzi, P. *et al*. Quantum espresso: a modular and open-source software project for quantum simulations of materials. *Journal of Physics: Condensed Matter* **21**, 395502, http://www.quantum-espresso.org (2009).
47. Giannozzi, P. *et al*. Advanced capabilities for materials modelling with quantum espresso. *Journal of Physics: Condensed Matter* **29**, 465901 (2017).
48. Perdew, J. P., Burke, K. & Ernzerhof, M. Generalized gradient approximation made simple. *Physical Review Letters* **77**, 3865 (1996).
49. Yagmurcukardes, M. *et al*. Pentagonal monolayer crystals of carbon, boron nitride, and silver azide. *Journal of Applied Physics* **118**, 104303, https://doi.org/10.1063/1.4930086 (2015).
50. Yu, R., Weng, H., Fang, Z., Dai, X. & Hu, X. Topological node-line semimetal and dirac semimetal state in antiperovskite $cu_3PdN$. *Phys. Rev. Lett.* **115**, 036807, https://doi.org/10.1103/PhysRevLett.115.036807 (2015).
51. Matsuura, S., Chang, P. Y., Schnyder, A. P. & Ryu, S. Protected boundary states in gapless topological phases. *New Journal of Physics* **15**, 065001 (2013).
52. Topp, A. *et al*. The effect of spin-orbit coupling on nonsymmorphic square-net compounds. *Journal of Physics and Chemistry of Solids* (2017).
53. Guan, S. *et al*. Two-dimensional Spin-Orbit Dirac Point in Monolayer HfGeTe. *Physical Review Materials* **1**, 054003, https://doi.org/10.1103/PhysRevMaterials.1.054003 (2017).
54. Klemenz, S., Lei, S. & Schoop, L. Topological semimetals in square-net materials. *Annual Review of Materials Research* **49** (2019).
55. Taherinejad, M., Garrity, K. F. & Vanderbilt, D. Wannier center sheets in topological insulators. *Physical Review B* **89**, 115102 (2014).
56. Soluyanov, A. A. & Vanderbilt, D. Wannier representation of Z2 topological insulators. *Physical Review B* **83**, 035108, https://doi.org/10.1103/PhysRevB.83.035108 (2011).
57. Marzari, N., Mostofi, A. A., Yates, J. R., Souza, I. & Vanderbilt, D. Maximally localized Wannier functions: Theory and applications. *Reviews of Modern Physics* **84**, 1419–1475, https://doi.org/10.1103/RevModPhys.84.1419 (2012).
58. Mostofi, A. A. *et al*. An updated version of Wannier90: A tool for obtaining maximally-localised Wannier functions. *Computer Physics Communications* **185**, 2309–2310, https://doi.org/10.1016/J.CPC.2014.05.003 (2014).
59. Soluyanov, A. A. & Vanderbilt, D. Smooth gauge for topological insulators. *Phys. Rev. B* **85**, 115415, https://doi.org/10.1103/PhysRevB.85.115415 (2012).
60. Gresch, D. *et al*. Z2Pack: Numerical implementation of hybrid Wannier centers for identifying topological materials. *Physical Review B* **95**, 075146, https://doi.org/10.1103/PhysRevB.95.075146 (2017).
61. Wu, Q., Zhang, S., Song, H.-F., Troyer, M. & Soluyanov, A. A. WannierTools: An open-source software package for novel topological materials. *Computer Physics Communications* **224**, 405–416 (2018).


## Acknowledgements

This work has been partially supported by Chilean CONICYT PhD scholarship No. 21150492, Chilean FONDECYT Grant No. 1151316 and the Spanish MINECO and the European Union under Grant No. FIS2015-64654 P/MINECO/FEDER, CSIC i-coop Grant No. ICOOPA-20150. J.D.C. thanks the Laboratorio de Simulación y Computación Científica at Universidad de Medellín for computational time.

## Author Contributions

S.B., M.P. and L.C. designed the research. S.B. and J.C. performed all the calculations. L.C. and M.P. provided theoretical support. All authors discussed the interpretation of the results and contributed to the writing to the manuscript.

## Additional Information

**Supplementary information** accompanies this paper at https://doi.org/10.1038/s41598-019-49187-w.

**Competing Interests:** The authors declare no competing interests.

**Publisher's note:** Springer Nature remains neutral with regard to jurisdictional claims in published maps and institutional affiliations.